Supplement of

Baseline ozone at northern midlatitudes: Continuing long-term decrease and shifts in seasonal cycle drive by decreasing anthropogenic precursor emissions

David D. Parrish, Charles A. Mims, Richard G. Derwent, Ian C. Faloona, Henry Bowman, Tongwen Wu, Jie Zhang, Makoto Deushi, Naga Oshima

Correspondence to: David D. Parrish (david.d.parrish.llc@gmail.com)

Contents of this file

Introduction This supporting information collects the parameter values derived from fits of Equation 1 time series of monthly mean baseline ozone concentrations analyzed in this work in Tables S1 and S2. Figures S1 to S9 illustrate some of these fits, provide additional data presentations, and illustrate some of the discussion points. Text S1 to S6 give further discussion of aspects of the data sets and analysis.

Table S1. Parameter values of fits of Equation 1 to monthly means of baseline ozone data sets. These parameter values quantify mean long-term changes over the available data records. The first two rows are MBL sites, the third (European alpine), fifth and sixth rows represent the FT, and the fourth row (Lassen NP) is a continental boundary layer site. Bottom two rows are fits to data from all eight data sets.

Data Set	a (ppb)	b (ppb yr^{-1})	c (10^{-3} ppb yr^{-2})	d (10^{-4} ppb yr^{-3})	year$_{max}$	time span of data
Mace Head	39.9 ± 0.7	0.29 ± 0.08	-21 ± 8	3 ± 5	2008.8 ± 3.3	4/87 - 5/22
Pacific MBL	32.7 ± 1.8	0.04 ± 0.17	-25 ± 22	8 ± 10	2000.8 ± 3.5	11/87 - 12/24
Lassen NP	41.2 ± 0.8	0.17 ± 0.08	-28 ± 10	8 ± 5	2003.5 ± 2.9	10/87 - 9/25
European alpine	51.3 ± 0.7	0.07 ± 0.09	-16 ± 3	5 ± 3	2002.6 ± 2.8	1/78 - 12/24
European FT [a]	56.5 ± 0.7	0.34 ± 0.17	-30 ± 22	7 ± 7	2008 ± 12	8/94 - 10/25
North American FT [a]	57.7 ± 0.7	0.06 ± 0.10	-24 ± 15	9 ± 5	2001.2 ± 1.6	1/92 - 9/25
All baseline data sets [b]	-0.2 ± 0.2	0. 14 ± 0.02	-15.5 ± 1.3	3.3 ± 0.8	2005.6 ± 1.7	1/78 - 10/25
2-yr averages [c]	-0.3 ± 0.8	0.12 ± 0.10	-14.6 ± 3.6	3.6 ± 2.7	2005.2 ± 5.1	1/78 - 10/25

[a] European FT and North American FT are fits, respectively, to the combined European sonde and IAGOS data sets, and to the combined Trinidad Head and Boulder sonde data sets; all are for 3 to 9 km altitude means.

[b] Results for normalized, deseasonalized monthly means from all eight data sets.

[c] Results for 2-yr averages of normalized, deseasonalized monthly means from all eight data sets.

Table S2. Parameter values of fits of Equation 1 to monthly means of baseline ozone data sets. These parameter values quantify the mean seasonal cycle for the first six data sets included in Table S1.

Data Set	a (ppb)	A_1 (ppb)	ϕ_1 (rad)	A_2 (ppb)	ϕ_2 [b] (rad)	number of monthly means	RMSD (ppb)
Mace Head	39.9 ± 0.7	5.9 ± 0.6	0.59 ± 0.10	3.0 ± 0.6	-2.38 ± 0.19	422	2.3
Pacific MBL	32.7 ± 1.8	5.8 ± 1.4	0.49 ± 0.24	3.4 ± 1.4	-2.3 ± 0.4	394	3.4
Lassen NP	41.2 ± 0.8	3.4 ± 0.7	-1.15 ± 0.20	2.3 ± 0.7	-0.2 ± 0.3	455	3.4
European alpine	51.2 ± 0.7	8.2 ± 0.7	-1.23 ± 0.08	(0.3 ± 0.7)	---	564	3.2
European sondes [a]	51.9 ± 1.1	7.3 ± 0.7	-1.25 ± 0.09	(0.4 ± 0.7)	---	333	2.4
IAGOS [a]	50.3 ± 1.1	8.0 ± 0.9	-1.21 ± 0.11	(0.7 ± 0.9)	---	344	3.5
Trinidad Head sondes [a]	53.6 ± 1.3	6.0 ± 0.9	-1.27 ± 0.15	(0.1 ± 0.9)	---	323	5.5
Boulder sondes [a]	56.3 ± 0.7	8.0 ± 0.6	-1.33 ± 0.07	(0.0 ± 0.6)	---	405	4.0

[a] These 4 FT fits are for the separate European sonde, IAGOS, Trinidad Head and Boulder sonde data sets; all are for 3 to 4 km altitude means.

[b] Results for ϕ_2 are given only if the value derived for A_2 is judged to be statistically significantly different from zero.

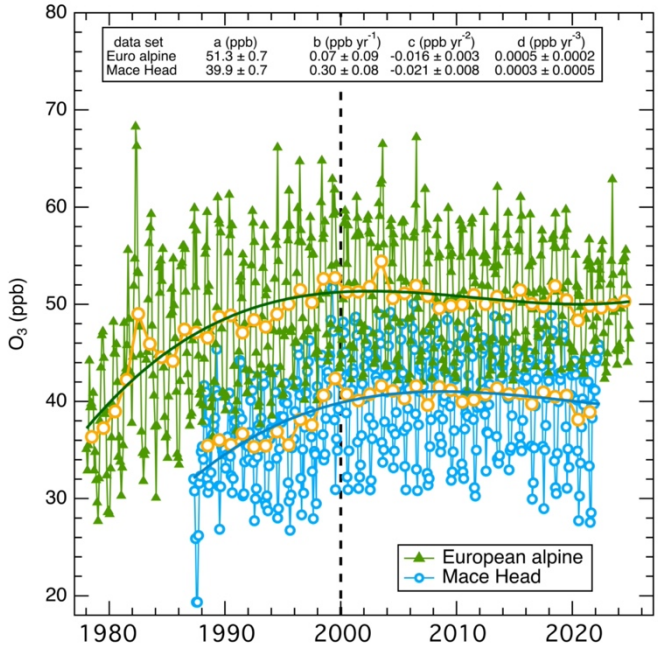

885

Figure S1: Time series of monthly and annual (orange symbols) mean ozone mixing ratios from the two European surface site data sets. The solid curves give the respective nonlinear, least-squares regression fits of the first four terms of Equation 1 to the monthly data, and the vertical dashed line indicates the origin of the time scale (year 2000) for those fits. The annotation gives the parameters of the fits.

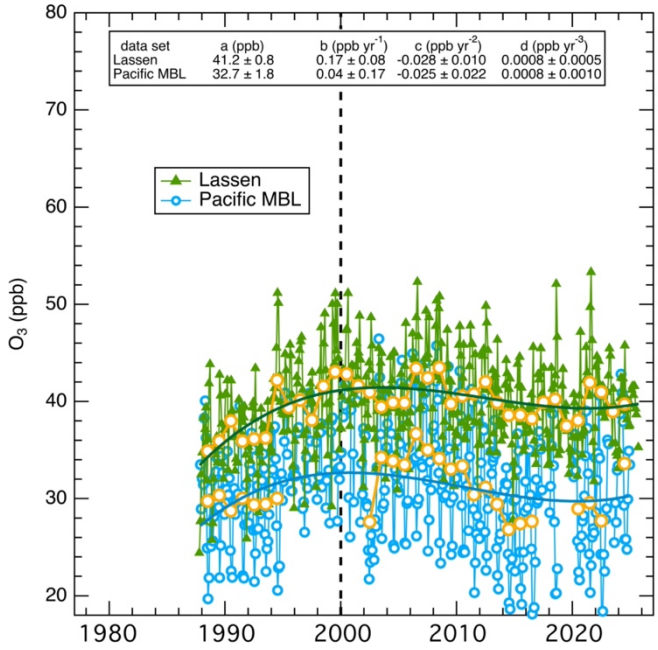

890 **Figure S2:** Time series of monthly and annual mean ozone mixing ratios from the two North American Pacific coast data sets. The figure is in the same format as Fig. S1.

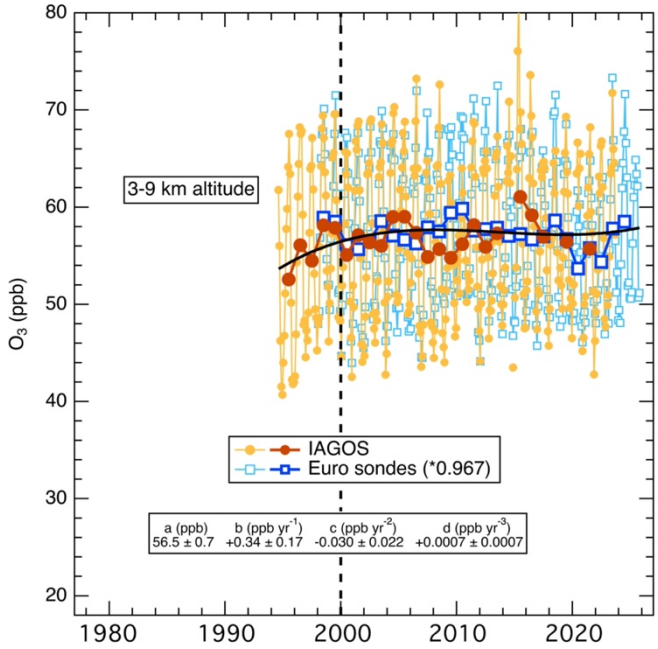

Figure S3: Time series of monthly (smaller symbols) and annual (larger symbols) mean ozone mixing ratios from the European sonde and IAGOS data sets averaged over the 3-9 km altitude interval. Sonde data are normalized to the IAGOS data as discussed in the text and indicated in the annotation. The solid curve gives the nonlinear, least-squares regression fit of the first four terms of Equation 1 to the means of the data sets, and the vertical dashed line indicates the origin of the time scale (year 2000) for that fit. The annotation gives the parameters of the fit.

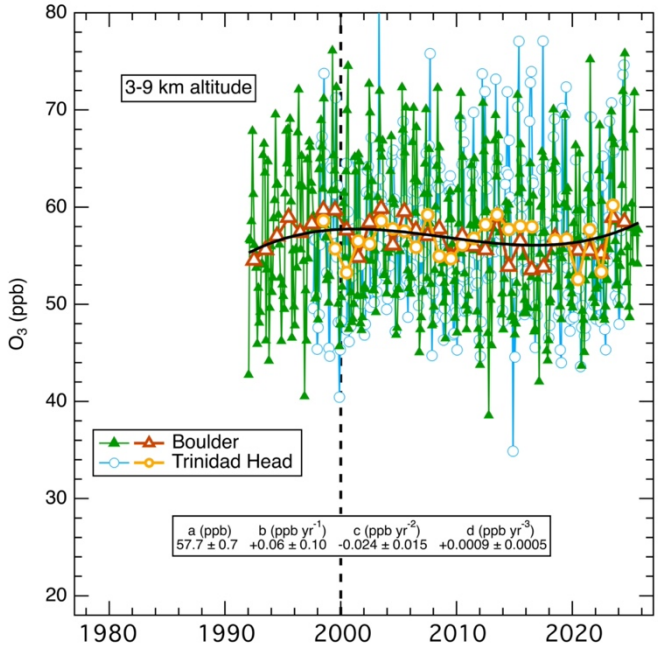

Figure S4: Time series of monthly and annual mean ozone mixing ratios from the Boulder and Trinidad Head sonde data. The figure is in the same format as Fig. S3.

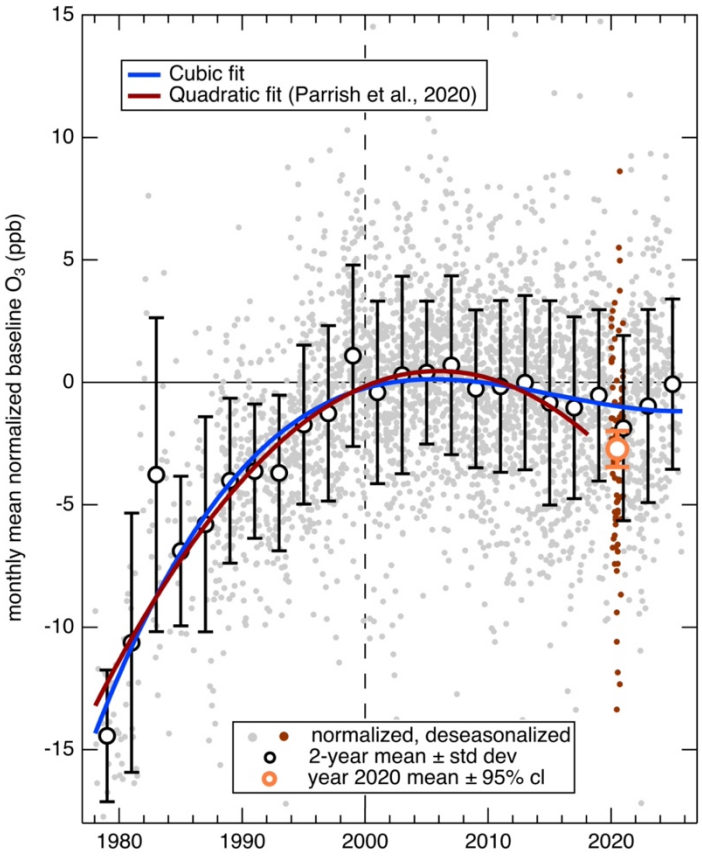

Figure S5: Data and cubic fit from Fig. 2 of the paper, with the quadratic fit from Parrish et al. (2020) added for comparison.

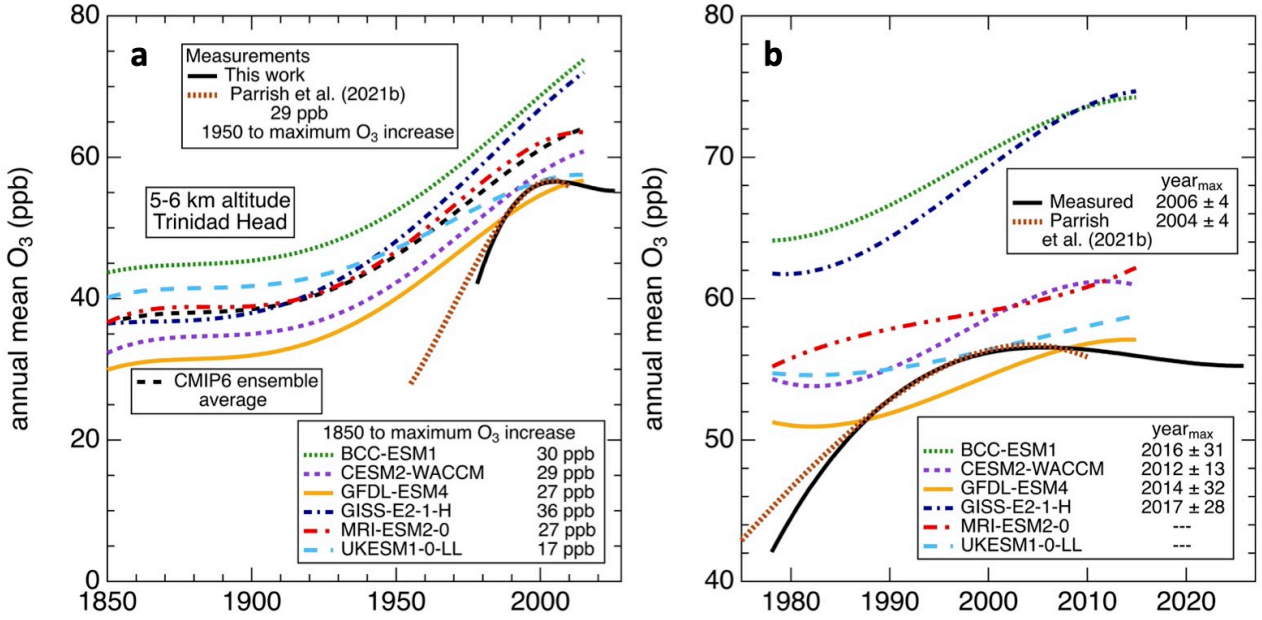

Figure S6: Similar comparison of long-term changes of baseline ozone as in Fig. 5 of the paper, but for model grid cells located 5 to 6 km altitude above Trinidad Head California. The measurements are normalized to the year 2000 intercept fit to mean baseline ozone measured over that altitude interval by sondes launched from Trinidad Head. The ensemble average for the six CMIP6 models is included in **a)**.

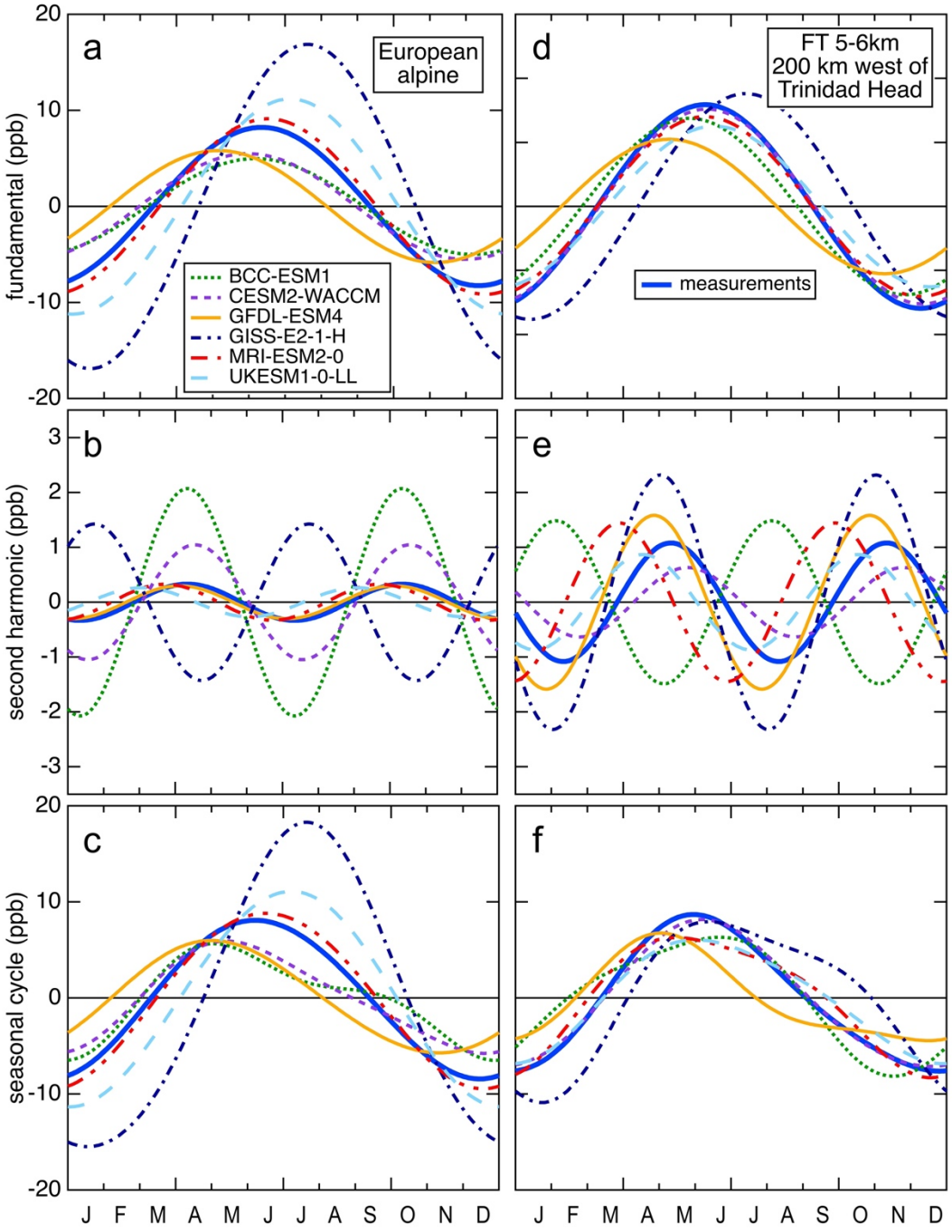

Figure S7. Harmonic analysis of baseline ozone seasonal cycles at the European alpine sites and 5-6 km altitude 200 km west (offshore) from the North American Pacific Coast at Trinidad Head CA. The fundamental harmonics are in **a)** and **d)**, the second harmonics in **b)** and **e)**, and their sum compared to Trinidad Head sonde measurements in **c)** and **f)**. In **f)** the measurements are indicated with a dashed line to indicate the difference in location of the measurements and model simulations.

S1. Estimation of recent baseline ozone concentrations at Trinidad Head surface site

At rural sites on the North American coast that receive air inflow from the marine boundary layer, measured ozone concentrations are reduced by ozone loss due to surface deposition. Selection of measurement data during periods of relatively high onshore winds allows the actual baseline ozone concentrations to be determined **(**Parrish et al., 2009). Baseline ozone concentrations were measured through this approach from the start of measurements in 2002 through 2017. However, no wind data are available from that site after 2017, so an alternative approach has been followed for the 2018-2024 data. Over the first 16 years of measurements, monthly means of wind-selected ozone data correlate well with monthly means of all data ($r^2 = 0.929$), but the ratio of the all data to the wind-selected means average only 0.890 ± 0.007. Consequently, during the final 7 years of the measurements, monthly mean baseline ozone is estimated from the monthly means of all measurements divided by 0.890 to approximately correct for the effects of surface deposition.

S2. Estimation of European alpine ozone concentrations in the 1930s and 1950s

Tarasick et al. (2019) collected historical ozone data and critically reviewed their accuracy. Some of those data, collected in the 1930s and 1950s at relatively elevated European sites, are comparable to the later measurements that constitute the European alpine data set considered here. The table below includes all data from Table 4 of Tarasick et al. (2019) collected between 1929 and 1975 at European sites above 1.5 km elevation. These data, together with the European alpine data set, can be utilized to approximately characterize the baseline ozone concentrations in the lower free troposphere over Europe for nearly an entire century (1930-2025). Three points should be noted regarding these early data. First, the 1930s measurements were made during short periods of a few days or less in different seasons; each of the six sets of measurements can be corrected to approximate the corresponding annual mean by subtracting the tabulated seasonal delta. The mean of these corrections is small (+0.6) but individual corrections very between -4.5 and +5.3 ppb. When these corrections are made and the results of the 6 studies are averaged (weighted by the number of measurement days, which is the approach used by Tarasick et al., 2019) the 1930s baseline ozone is estimated as **27.3 ± 1.8** (mean ± std. dev) ppb. It is notable that the seasonal corrections reduce the variance of the 6 studies by nearly a factor of 3. Second, the 1950s measurements provide much better temporal coverage, but more limited elevation and spatial range than the 1930s data. Third, the 1950s Arosa data were one of the primary determinants of the lower extent of the polynomial fit from Parrish et al. (2021b) included in Figs. 5 and S6.

Table S3. Ozone measurement data from the 1930s and 1950s collected at elevated European sites (Tarasick et al., 2019).

Location	Date	Days of data	Mean ± Std. Dev. (ppb)	Seasonal delta (ppb) [a]
Arosa 1.86 km	30 April 1930	1	32.2	+4.5
Arosa 1.86 km	Sept. 1932-Apr. 1933	5	24.9 ± 10.5	-5.3
Arosa 1.86 km	March-May 1934	11	28.2 ± 2.8	+3.4
Jungfraujoch 3.45 km	18-31 August 1933	7	30.9 ± 5.6	+2.3
Mt. Ventoux 1.91 km	October 1938	1	25.5	-3.4
Jungfraujoch 3.45 km	August 1938	5	30.0	+2.3
1930s mean		**30**	**28.6 ± 3**	**+0.6 ± 4**
Arosa 1.86 km	Apr. 1950-July 1951	400	26.4 ± 6.2	---
Arosa 1.86 km	Apr. 1954-Oct. 1958	1500	23.2 ± 6.4	---
1950s Weighted mean		**1900**	**23.8 ± 6**	---

[a] The seasonal delta is calculated from the preindustrial seasonal cycle derived from the analysis of the seasonal cycle shift at the European alpine sites, i.e., seasonal delta = A_1^0 * sin(χ + ϕ_1^0) for the parameter values given in Fig. 4a.

S3. Further discussion of analysis approach and methods

Tropospheric ozone varies widely on time scales ranging from minutes to decades and longer, and on spatial scales ranging from < 1 kilometer to hemisphere-wide. Higher frequency variability can obscure the long-term changes and seasonal cycles that are the subject of the present analysis. To maximize the accuracy and precision of our desired quantifications, it is necessary to average, as fully as possible, over this obscuring temporal variability. The seasonal cycle is the shortest time scale of our focus, so we average each data set to give representative monthly means. We desire results characteristic of the background troposphere, so we average separate baseline representative data sets over the largest spatial scales that are characterized by homogeneous results; this spatial averaging is discussed further in Section 3.

The data sets are analyzed following the procedures of Parrish et al. (2020). Generally all monthly means derived from the complete data records are included in the analysis. In the calculation of these means, measured ozone mixing ratios larger than 150 ppb are excluded from the sonde and IAGOS data sets. These high concentrations are believed to represent sporadic stratospheric intrusions, and are excluded from the analysis, which is aimed at characterizing baseline tropospheric ozone. For seasonal cycle analysis the ozone profiles measured by the sondes and the IAGOS aircraft are averaged from 3 to 4 km altitude so that the results can be directly compared to the European alpine data set, which is collected at sites whose elevations are in this range.

The four FT data sets over Europe (European sondes and IAGOS) and North America (Boulder, Colorado and Trinidad Head, California sondes) are shorter than the other four data sets, so fits to the individual data sets give power series parameter values with larger confidence limits. Two approaches are taken to improve the precision of the derived parameter values. First, the sonde and IAGOS data over a large (3 to 9 km) altitude range are averaged to maximize the amount of data upon which the FT analysis is based. Second, the two FT data sets over each continent are averaged into the European FT

and North American FT data sets, respectively, to further improve the precision of the analysis. A regression analysis indicates no significant bias (regression slope = 0.99 ± 0.01 with intercept set to zero) between the two North American FT data sets, so monthly means were averaged if means were available from both data sets; the Boulder mean alone was used for the periods without Trinidad Head data. The European sonde data and the IAGOS data were similarly averaged, except, as discussed by Parrish et al. (2020), the European sonde data are systematically larger than the IAGOS data. Tarasick et al. (2019) suggest that the IAGOS data should be considered the reference data set. Accordingly, based on the correlation of monthly means between these data sets, the European sonde data were reduced by 3.3% before averaging; these normalized data are plotted in all figures. It should be noted that year 2020 monthly means are included in the long-term change analysis even though those data may have been impacted by reduced anthropogenic emissions driven by societal efforts to control the COVID-19 pandemic; Section 3.2 examines those possible impacts.

S3.1 Mathematical description of long-term changes and seasonal cycles

We simultaneously quantify the long-term changes and seasonal cycle of baseline ozone by fitting a power series expansion to the long-term change and a Fourier series expansion to the seasonal cycle. A power series can quantify any continuous, time varying function without a priori knowledge of the underlying functional form, and the Fourier series can quantify any temporally repeating function, such as the seasonal cycle. Parrish et al. (2019) describe this approach in detail. Simultaneous quantification of the long-term changes and seasonal cycle is utilized so as to minimize the uncertainties in the fits. In this work, we effect this quantification through a least-squares fit of ozone monthly means to Equation 1,

$$O_3(t) = a + bt + ct^2 + dt^3 + A_1*\sin(\chi + \phi_1) + A_2*\sin(2\chi + \phi_2), \quad (1)$$

where t is time in years relative to the year 2000 (i.e., t = year-2000). The seasonal cycle variable, χ, spans one year's time period in radians from 0 to 2π, i.e., $\chi = 2\pi t$, beginning from zero at the start of each year.

The first four terms of Equation 1 are a cubic polynomial, which constitutes the first four terms of the power series. The coefficients of those terms quantify the long-term change of average ozone mixing ratios. One advantage of using fits to a power series to quantify long-term ozone changes is that simple calculus manipulations provide direct physical interpretations of derived coefficient values:

- ***a*** is the interpolated annual mean ozone mixing ratio in the reference year 2000; units: ppb.
- ***b*** is the slope of the trend in mean ozone mixing ratio in that reference year; units: ppb yr^{-1}.
- ***c*** is the curvature of the fit, which is one-half of the rate of change of the trend slope, in 2000; units: ppb yr^{-2}.
- ***d*** is one-sixth of change in the curvature of the fit; units: ppb yr^{-3}; with only four terms included in the power series fit, this quantity is constant throughout the fitted time period.

Additional power series terms, i.e., et^4 + …, would be included in the fit to any data set that statistically justified that inclusion; however, none of the fits to the data sets examined in this work requires inclusion of a term of order higher than the cubic term. Examples of cubic polynomial fits to monthly mean ozone concentrations in all individual data sets

considered in this work are illustrated in Figs. S1-S4. Previous analyses (e.g., Logan et al. 2012; Parrish et al. 2020) have demonstrated that baseline ozone at northern midlatitudes increased during early decades of available measurement data, reached a maximum during the decade of the 2000s, and has since decreased. The polynomial of Equation 1 captures this behavior, and the parameter values derived in fits of that equation allow calculation of the year that maximum was reached,

$$\text{year}_{max} = [-c \pm (c^2 - 3bd)^{1/2}]/3d + 2000, \quad (2)$$

for the full cubic polynomial, or a simpler equation,

$$\text{year}_{max} = -b/2c + 2000, \quad (3)$$

if the quadratic polynomial provides an adequate fit to the measurement data. Standard propagation of error techniques allow calculation of confidence limits for year_{max} for either equation.

The last two terms of Equation 1 are the first two terms of a Fourier series: the fundamental (i.e., a single sine cycle per year) and the second harmonic (i.e., two sine cycles per year). The two terms have four parameters that quantify the seasonal cycle – the amplitudes (A_1 and A_2 in ppb) and phases (ϕ_1 and ϕ_2 in radians) of the two terms. In the fits to the data sets investigated in this work, only one or two harmonic terms are generally statistically justified; higher order harmonics, which could be included if statistically justified, are not considered in this work.

Fits of Equation (1) quantify the average seasonal cycle over the time period spanned by the fitted data. However, in favorable cases Bowman et al. (2022) find that inclusion of two Gaussian functions can separately describe the shifts in the magnitude and phase of the fundamental of the seasonal cycle; these are added to the A_1 and ϕ_1 parameters in Equation 1:

$$A_1 = A_1^0 + r*\exp\{-((t-m)/s)^2\}, \quad (4)$$

$$\phi_1 = \phi_1^0 + r_\phi*\exp\{-((t-m_\phi)/s_\phi)^2\}. \quad (5)$$

Equations 4 and 5 quantify the shift in the amplitude and phase of the seasonal cycle, respectively. The r and r_ϕ parameters define the magnitude of the Gaussian functions (i.e., the maxima of the shifts in ppb and radians, respectively), the m and m_ϕ parameters give the times (in years relative to 2000) that those maxima were reached, and the s and s_ϕ parameters quantify the widths in years of the functions. Gaussian functions are included only in the fundamental term because, first, that harmonic accounts for the large majority of the seasonal cycle for all data sets from which the shifts can be quantified, and second, it is the only harmonic that was seen to consistently shift across different locations and model simulations. Note that in these equations, the A_1^0 and ϕ_1^0 parameters characterize the amplitude and phase of the preindustrial seasonal cycle, since the Gaussian terms contribute negligibly before ~1900.

Most of the analyses in this work are based upon fits of Equation 1 to the data sets summarized in Section 2.1. In Section 3.4, we investigate long-term shifts in the baseline ozone seasonal cycle for one data set; for this analysis, Equations 4 and 5 are substituted into Equation 1 to derive the fitting equation:

$$O_3(t) = a + bt + ct^2 + dt^3 + (A_1^0 + r*\exp\{-((t-m)/s)^2\})*\sin(\chi + \phi_1^0 + r_\phi*\exp\{-((t- m_\phi)/s_\phi)^2\}) + A_2*\sin(2\chi + \phi_2). \quad (6)$$

In this analysis, the fit of Equation 6 to only one of the ozone time series gave statistically significant parameter values for the parameters of the Gaussian functions. The fit for this particular data set, the fit to Equation 6 gave statistically significant values for 12 of the 14 parameters, but the second harmonic did not make a significant contribution. Further, $m_\phi = m$ and $s_\phi = s$ within the derived confidence limits; this equivalence is expected if the shifts in the magnitude and phase of the fundamental arise from the same physical cause, such as changing anthropogenic emissions. Accordingly, the final analysis of this data set is simplified by reducing Equation 6 to Equation 7 with 10 parameter values:

$$O_3(t) = a + bt + ct^2 + dt^3 + (A_1^0 + r*\exp\{-((t-m)/s)^2\})*\sin(\chi + \phi_1^0 + r_\phi*\exp\{-((t-m)/s)^2\}). \quad (7)$$

S3.2 Confidence limits and interpretation of statistical significance

It is our experience that the scientifically useful information that can be extracted from the analysis described in the preceding section is limited by the uncertainty of the derived parameter values. Consequently, we focus considerable attention both on deriving realistic confidence limits and on minimizing the uncertainty reflected in those confidence limits. In general, 95% confidence are calculated, unless indicated otherwise. The following paragraphs discuss three issues considered in our analysis of statical uncertainties.

In order to fit Equation 1 or Equation 6 to a time series of monthly mean concentrations, the fitting procedure must optimize values for 8 or 14 parameters, respectively. Standard least-squares fitting procedures can readily perform such optimizations, thereby providing parameter values with associated confidence limits. However, in general, as the number of derived parameter values increases in fits of equations to time series of observational data, the confidence limits of all parameters can widen so rapidly that the results become of little utility. In this work the terms in the power series do suffer from this effect, but the situation is not as difficult as might be expected. Four power series terms are used, so our analysis is to some extent limited by relatively wide confidence limits - close attention will be paid to this issue. In contrast, the terms of the Fourier series are orthogonal functions. Fits of orthogonal functions to data sets derive the separate coefficient values from information in the data set that is independent for each function; in this case the confidence limit of each derived coefficient value is independent of the number of Fourier series terms included in the fit. Although the Fourier series terms are not formally orthogonal to the power series terms, those former terms vary rapidly on the seasonal time scale compared to the relatively slow decadal time scale variation of the latter terms. As a consequence, deriving the seasonal cycle parameters from the Fourier series, and the additional coefficients in the seasonal cycle fits included in Equations 4-6, have little effect on the confidence limits of the power series coefficients.

The confidence limits provided by standard least-squares fitting procedures can be underestimated, often by large factors, which can lead to overly optimistic interpretation of derived parameter values. This situation arises because the fitting routines implicitly assume that each data point is statistically independent of all other data points. However, time series of ozone concentrations often suffer from a high degree of autocorrelation, resulting in much less robust data sets than might be expected from the number of data. This autocorrelation is both temporal and spatial. Atmospheric cycles in meteorological

and transport processes, which affect ozone concentrations, operating on scales of hours to decades cause temporal correlation of measured ozone concentrations over that full temporal spectrum. Ozone concentrations can also so be correlated over spatial scales extending up to hemispheric scales, so that measurements from widely separated locations cannot be considered to be statistically independent. Our approach to effectively dealing with this autocorrelation issue is two-fold. First, we average over as wide spatial and temporal ranges as consistent with derivation of our desired information, i.e., ozone long-term changes and seasonal cycles at northern mid-latitudes. Second, we use statistical techniques as described in Parrish et al. (2019) to evaluate the autocorrelation that remains in the averaged data sets that we analyze, and to appropriately widen the quoted confidence limits to correct for this effect.

The extent of spatial and temporal averaging that we employ is guided by the confidence limits derived in the analysis of individual data sets. If the separate analysis of two or more data sets yield parameter values that agree within their derived confidence limits, then they are considered to be candidates for averaging together into a single data set if that averaging does not compromise needed spatial resolution of the final analysis. There is some subjectivity in averaging decisions, since we wish to consider as many independent analyses as possible.

S4. Well-mixed free troposphere approximation

The concept used in this paper of a well-mixed free troposphere (FT) serving as a monitor for the entire zone is a valuable simplifying concept, but an approximate one. We test this concept and its relevance to the current study by simulating all compartment ozone concentrations in the 5 decadal years utilizing a previously published (Mims et al., 2022) simple compartmental model that is briefly described in Section 4.5 of the paper. The circular flow around the FT circuit is not infinitely fast, so irregularities in the flux from the underlying boundary layer compartments can produce modest irregularities in the FT ozone concentration. Figure S8 shows the model results for the FT and MBL model compartments. In all five decadal years the annual mean ozone in the 9 FT compartments agree with their mean with a standard deviation < 0.9 ppb indicating that the FT is quite well-mixed, with only small systematic differences remaining. The only source of ozone to the MBL included in the model is transport from the FT, so there is near-perfect correlation between the ozone in the FT and underlying MBL pairs of compartments, with the MBL concentration 75.5% of that in the FT.

The differing photochemical production among the boundary layer compartments produces uneven contributions to the FT above those compartments. Consequently, as a result of the long-term shift in regional emissions over the past 40 years, the maximum FT ozone has shifted from over North America and Europe to over East Asia and western North America. As a result, the western North American FT compartment, being the closest continent downstream of East Asia, has a small upward bias in its long-term change compared to the zonal average, while the European compartment, being the closest downstream of a now relatively clean North America, has a similar downward bias in its long-term change. Such biases will affect the analyzed maximum year in regression fits for particular sites. The effect of short-term events with global extent, such as the Covid-19 pandemic, should be apparent and give similar ozone transients in all regions.

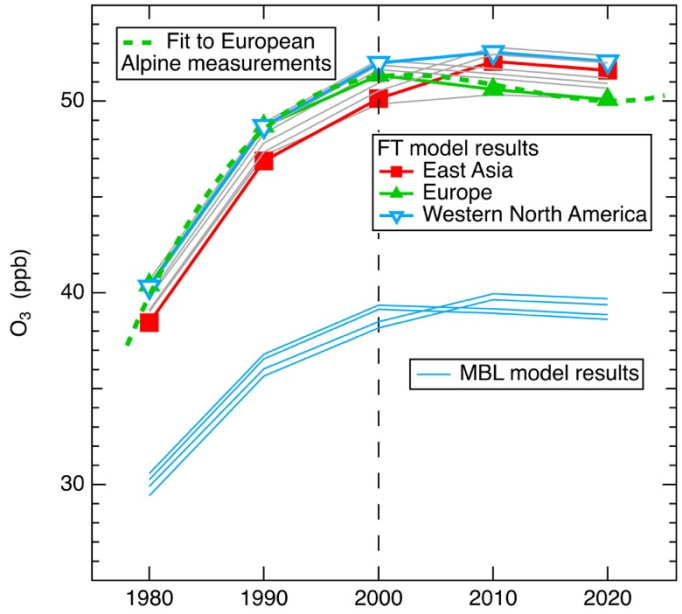

Figure S8. Comparison of model calculated FT and MBL ozone concentrations compared to the fit to the European alpine data set from Figs. 1 and S1. Results for 3 FT compartments are indicated by colored lines and points as indicated in the annotation; the other 6 FT compartment results are shown as light grey lines, The 4 MBL compartment results are shown as light blue lines.

S5. Contribution of 3rd harmonic to ozone seasonal cycle in the free troposphere

Fourier transforms of ozone monthly means in the FT reveal that the 3rd harmonic makes a small contribution to the seasonal cycle that is on the edge of statistical significance in some data sets. Figure S8 shows the Fourier transform of the monthly mean data from the European alpine sites. The fundamental contribution (peak at frequency = 1 yr^{-1}) dominates the seasonal cycle as discussed in Sections 3.3 and 4.3, and illustrated by the solid line in Fig. S9. The 3rd harmonic contribution flattens both the seasonal maximum and minimum, and steepens the transitions between those extremes. Table S4 indicates that the 3rd harmonic contribution makes a statistically significant contribution at the 95% confidence level to the seasonal cycle at two of the five FT data sets. The significance of this contribution can be judged by the RMSDs of the data about the fitted curves in Figure S9; those values are 3.23 ppb for the fundamental and 3.16 ppb for the fundamental plus 3rd harmonic.

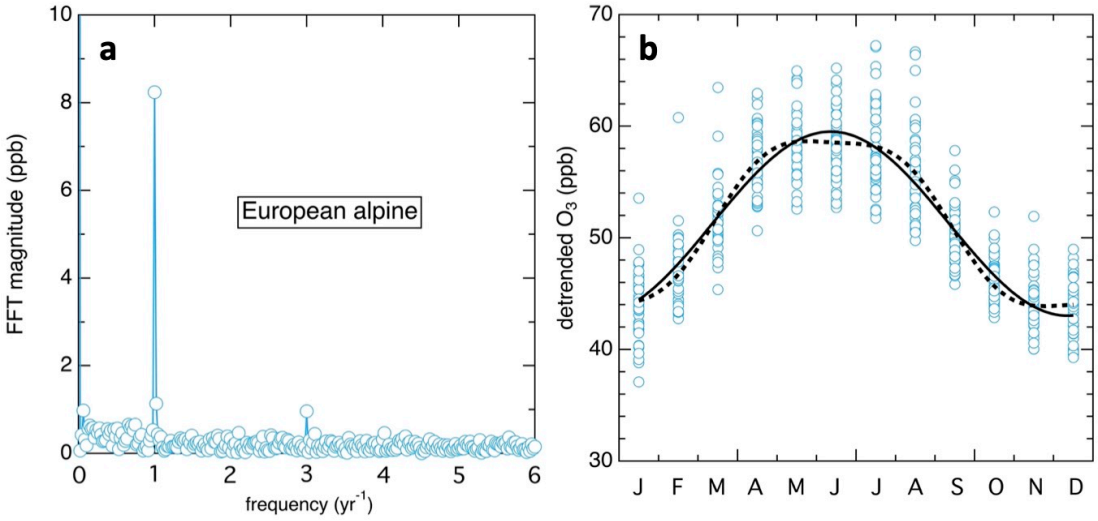

Figure S9. Harmonic analysis of baseline ozone seasonal cycles at the European alpine sites. **a**) Fourier transform results. **b**) Detrended monthly means and fits to the fundamental harmonic (solid curve) and the sum of the fundamental and third harmonic (dotted line). Both curves are offset by the year 2000 intercept (*a* parameter value).

Table S4. Parameter values of fits of Equation 1 to detrended monthly means of baseline ozone data sets.

Data Set	*a* (ppb)	A_1 (ppb)	ϕ_1 (rad)	A_3 (ppb)	ϕ_3 [b] (rad)
European alpine	51.3	8.2 ± 0.7	-1.23 ± 0.08	1.0 ± 0.7	+2.44 ± 0.70
European sondes [a]	51.9	7.3 ± 0.7	-1.25 ± 0.09	(0.5 ± 0.7)	---
IAGOS [a]	50.2	7.9 ± 0.9	-1.21 ± 0.11	(0.6 ± 0.9)	---
Trinidad Head sondes [a]	53.4	6.0 ± 0.9	-1.27 ± 0.15	(0.2 ± 0.9)	---
Boulder sondes [a]	56.5	8.0 ± 0.6	-1.33 ± 0.07	1.9 ± 0.6	+2.60 ± 0.37

[a] These 4 FT fits are for the separate European sonde, IAGOS, Trinidad Head and Boulder sonde data sets; all are for 3 to 4 km altitude means.

[b] Results for ϕ_3 are given only if the value derived for A_3 is judged to be statistically significantly different from zero.

S6. Comparison of NO_X-rich versus NO_X-poor fast photochemical balance in the background free troposphere

Jeffries and Tonnesen (1994) describe an analysis of the fast photochemistry in any reaction system with a view to understanding how atmospheric chemistry works at the chemical process level. This fast photochemistry of the background FT involves two main free radical species: the hydroxyl (OH) radical and the peroxy radical (HO_2 + RO_2) pool and six main interrelated reaction processes:

- OH radical direct sources (for example, ozone photolysis via $O^1D + H_2O$)
- Peroxy radical direct sources (for example, formaldehyde photolysis)
- OH radical direct sinks (for example, OH + NO_2 + M)
- Peroxy radical direct sinks (for example, HO_2 + HO_2 + M)
- OH to peroxy radical interconversions (for example, OH + CH_4)
- Peroxy radical to OH interconversions (for example, HO_2 + NO or HO_2 + O_3).

Here, we focus on the OH to peroxy radical pool interconversion processes and their relationship with the photochemical production and destruction of tropospheric ozone in the FT. The important species that drive the major OH to peroxy radical pool interconversion processes are listed in Table S5. They include inorganic species - carbon monoxide (CO), hydrogen (H_2), ozone (O_3) and hydrogen peroxide (H_2O_2) - and organic species - methane (CH_4), formaldehyde (HCHO), methyl hydroperoxide (CH_3O_2H), ethane (C_2H_6) and propane (C_3H_8). The table gives representative mixing ratios for each trace gas in the northern hemisphere mid-latitude FT, together with the rate coefficients at a representative FT temperature (244 K) for their reactions with OH radicals. These data allow estimation of the OH loss rate coefficients for reactions with each trace gas. Altogether, the sum of the OH loss rate coefficients for the OH to radical pool interconversion processes amounts to 0.46 s^{-1}, corresponding to an OH removal lifetime of about two seconds.

Table S5. Representative trace gas mixing ratios, their OH reaction rate coefficients at 244K and the corresponding OH loss rate coefficients in the northern hemisphere mid-latitude FT.

Trace gas	Typical mixing ratio (ppb)	k_{OH} (10^{-12} cm^3 s^{-1})	OH loss rate (s^{-1})
CO	100	0.24	0.31
CH_4	1900	0.0017	0.040
H_2	530	0.0018	0.010
O_3	60	0.036	0.030
H_2O_2	0.5	1.7	0.010
HCHO	0.3	9.2	0.036
CH_3O_2H	0.1	8.6	0.011
C_2H_6	1.28	0.115	0.002
C_3H_8	0.26	0.69	0.002
total			0.46

Note: The average OH number density is assumed to be 10^6 molecule cm^{-3}.

Two conclusions may be drawn from Table S5:

- Whatever the role proposed for methane in the fast photochemistry of the free troposphere, it should be seen in the context of the role played by carbon monoxide.
- Likewise, whatever the role proposed for VOCs in the fast photochemistry of the free troposphere, it should be seen in the context of that played by methane.

The single largest contribution from any trace gas to OH to peroxy radical pool interconversion arises from the reaction of OH with CO:

$$OH + CO + O_2 \rightarrow HO_2 + CO_2, \quad \text{(S1)}$$

which is rapidly followed by the HO_2 radical reacting with nitric oxide (NO) or ozone to recycle the OH radical:

$$HO_2 + NO \rightarrow NO_2 + OH, \quad \text{(S2a)}$$

$$HO_2 + O_3 \rightarrow 2O_2 + OH. \quad \text{(S2b)}$$

For the reactions with organic species, the largest contributions arise from the reaction of OH with methane and formaldehyde:

$$OH + CH_4 + O_2 \rightarrow CH_3O_2 + H_2O. \quad \text{(S3)}$$

$$OH + HCHO + O_2 \rightarrow HO_2 + CO + H_2O. \quad \text{(S4)}$$

The reaction of OH with methane proceeds by way of the methyl peroxy radical (CH_3O_2).

The fate of the methyl peroxy radical differs in NOx-rich and NOx-poor environments. If NOx is plentiful, CH_3O_2 predominantly reacts with NO:

$$CH_3O_2 + NO \rightarrow CH_3O + NO_2. \quad \text{(S5)}$$

The methoxy radical (CH_3O) product reacts with oxygen to form the HO_2 radical, which is recycled back to OH:

$$CH_3O + O_2 \rightarrow HO_2 + HCHO \quad \text{(S6)}$$

$$HO_2 + NO \rightarrow NO_2 + OH. \quad \text{(S2a)}$$

Alternatively, if NOx is absent, CH_3O_2 reacts with HO_2 to form methyl hydroperoxide (CH_3O_2H)

$$CH_3O_2 + HO_2 + M \rightarrow CH_3O_2H + O_2. \quad \text{(S7)}$$

Reaction (S7) removes two peroxy radicals from the pool. The CH_3O_2H product either reacts with the OH radical to form the CH_2O_2H radical which is recycled back to OH:

$$CH_3O_2H + OH \rightarrow H_2O + CH_2O_2H \quad \text{(S8)}$$

$$CH_2O_2H \rightarrow HCHO + OH, \quad \text{(S9)}$$

or photolyzes to form the methoxy radical (CH_3O) and OH; CH_3O then forms formaldehyde and the HO_2 radical through reaction S6. Reactions (S6) and (S9) constitute the predominant formaldehyde source to the background free troposphere.

With these rapid reactions following the OH attack on each trace gas, the overall result in a NOx-rich environment is the cycling of the OH radical through the peroxy radical pool and back to OH, with nitric oxide (NO) being oxidized to nitrogen dioxide (NO_2). It is photolysis of the NO_2 product that provides the source of ozone (O_3), through:

$$NO_2 + h\nu \rightarrow NO + O \quad \text{(S10)}$$

$$O + O_2 + M \rightarrow O_3 + M \quad \text{(S11)}$$

The overall result in an environment lacking NOx is again the cycling of OH through the peroxy radical pool and back to OH, but with a loss of radicals in the formation of CH_3O_2H, and with O_3 lost in Reaction 2b.

An upper limit to the ozone production rate through reactions (S10) and (S11) can be derived from the OH to peroxy radical pool interconversion flux by assuming that all the peroxy radicals formed recycle through reaction (S2a); similarly, an upper limit to the ozone loss rate can be derived by assuming that all the peroxy radicals formed recycle through reaction (S2b). Table S6 summarizes the calculation of these upper limits, which is based on the rate of the OH reaction with each trace species (taken from Table S5) multiplied by the number of peroxy radicals produced in that OH reaction. Here we assume that a single HO_2 radical is produced in the oxidation of each inorganic species (CO, H_2, O_3, H_2O_2). For CH_4 we include only the primary OH attack and subsequent rapid reactions (i.e., reactions (S3) followed by (S5) and (S6) for NOx-rich conditions and (S3) followed by (S7) to (S9) if NOx is absent); this is necessary because HCHO is treated separately, and it is a product of both reaction sequences. Similarly, for HCHO we consider only the primary OH attack, reaction (S4), because the product CO is considered separately. Since formation of CH_3O_2H is not important in NOx-rich conditions and its formation and loss are included in the primary OH attack on CH_4 and the subsequent rapid reactions if NOx is absent, its ozone formation potential is assumed to be zero in both environments. The OH oxidation of C_2H_6 and C_3H_8 is assumed to produce the number of ozone molecules equal to the number of C – H bonds in NOx-rich conditions, but to destroy no ozone molecules during the primary OH attack if NOx is absent, as is the case for methane. Finally, it is necessary to account for 1 ozone directly lost in the OH reaction with O_3. On this basis, the total ozone production and destruction rates are estimated as 3.3 and 2.9 ppb per day, respectively. The oxidation of methane accounts for 36% and 21% of the total production and loss rates, respectively, when the 13% of the CO, 55% of the H_2 and 100% of HCHO (i.e., the secondary products of CH4 oxidation) are included with the contribution from the primary OH attack on CH_4. It is concluded the methane oxidation is potentially either an important source or an important sink of ozone in the northern hemisphere mid-latitude free troposphere, and that balance between production and loss depends upon the NOx concentration in the photochemical environment, with loss dominating at lower NO concentrations and formation dominating at higher NO concentrations. The breakeven point for ozone formation and loss occurs when the rates of Reactions (S2a) and (S2b) are equal; at 244K and 60 ppb O_3 in the FT, that equality is reached when the diurnal mean concentration of NO is ~8 ppt, which corresponds to approximately 20 to 40 ppt NOx, depending upon ambient conditions. One final note: the above chemistry does not include direct photolytic loss of O_3, when the $O(^1D)$ product reacts with H_2O to form 2 OH radicals; that O_3 loss process is not considered here.

Table S6. Estimation of the ozone production or destruction rate in the northern hemisphere mid-latitude free troposphere for NOx-rich and NOx-poor conditions.

Trace gas	OH loss rate (s^{-1})	Number of peroxy$_2$ radicals per trace gas molecule oxidized		Rate (ppb day^{-1})	
		O_3 produced if NOx-rich	O_3 lost if NOx absent	O_3 production if NOx-rich	O_3 destruction if NOx absent
CO	0.31	1	1	2.07	2.07
CH_4	0.040	2	0	0.59	0.0
H_2	0.010	1	1	0.064	0.064
O_3	0.030	0	2	0.0	0.37
H_2O_2	0.010	1	1	0.073	0.073
HCHO	0.036	1	1	0.28	0.28
CH_3O_2H	0.011	0	0	0.0	0.0
C_2H_6	0.002	6	0	0.076	0.0
C_3H_8	0.002	8	0	0.124	0.0
total	0.46			3.3	2.9

Reference

Jeffries, H., and Tonnesen, S.: A comparison of two photochemical reaction mechanisms using mass balance and process analysis, Atmos. Environ., 28 (18), 2991-3003, https://doi.org/10.1016/1352-2310(94)90345-X, (1994).

Table S7. Pacific MBL data set monthly and annual mean ozone data. This data set includes measurements from Redwood NP, CA (Nov. 1987 – May 1995); Olympic NP, WA (May 1991 – Dec. 2004); Pt. Reves NS, CA (June 1988 – Nov. 1992) and Trinidad Head, CA (Apr. 2002 – Dec. 2024).

year	Jan	Feb	Mar	Apr	May	Jun	Jul	Aug	Sep	Oct	Nov	Dec	Annual
1987											33.50	28.93	
1988	32.06	31.45	38.30	40.08	36.26	24.92	19.70	21.85	29.96	25.09	31.84	25.64	29.76
1989	28.16	32.33	32.77	34.19	34.32	29.09	21.86	25.18	34.37	32.68	30.94	28.38	30.36
1990	29.54	30.96	34.88	30.39	32.11	24.66	22.55	21.90	28.84	31.05	28.39	29.89	28.76
1991	30.29	30.50	36.63	39.53	35.74	28.99	22.07	21.83	27.31	31.41	28.85	27.41	30.05
1992	27.50	33.50	32.85	36.75	35.11	26.75	21.47	24.34	26.84	31.30	26.92	29.19	29.38
1993	28.46	34.59	31.87	34.60	33.13	26.33	22.52	24.85	25.60	28.36	31.21	31.84	29.45
1994	30.29	33.00	37.21	37.42	34.11	27.20	20.56	22.88	23.06	32.45	32.56	29.83	30.05
1995	31.75	35.89	40.87	40.08	34.57				30.81	30.79	32.31	33.09	
1996	32.50	32.33	36.75	36.83	37.34				29.00	29.67	26.55	31.83	
1997	34.20	31.07	39.13	40.86	35.93				14.09		35.80	29.92	
1998	31.38	32.25	36.82	37.73	31.20				29.04	31.88		32.94	
1999	27.50	36.88	38.09	38.33	34.41				27.69	33.13	32.00	33.26	
2000	34.74		38.41	39.61	41.79				30.11	26.07	39.14		
2001	34.60	29.67	41.39	41.30	40.04				27.58	33.63	30.44	37.23	
2002	36.63	36.45	29.52	29.20	24.69	21.73	23.46	26.24	24.71	27.24	23.70	27.84	27.62
2003	27.15	33.23	40.70	46.44	42.51	36.63	25.89	29.02	29.50	30.86	33.81	35.27	34.25
2004	37.71	36.83	40.42	39.70	36.71	34.40	25.21	24.92	33.01	32.28	31.25	33.97	33.87
2005	30.66	35.61	41.93	44.25	38.27	32.60	25.45	25.32	29.51	29.79	35.25	33.41	33.50
2006	41.95	39.13	44.92	42.41	42.21	34.24	26.16	29.47	29.96	34.58	41.54	33.61	36.68
2007	33.24	39.33	40.83	44.04	41.91	31.89	24.61	27.81	33.78	30.92	34.73	37.00	35.01
2008	37.51	35.51	42.11	45.74	40.19	32.64	25.45	23.36	30.81	31.44	30.11	34.92	34.15
2009	30.37	40.67	41.52	43.58	35.14	29.60	24.25	25.12	30.17	31.58	32.59	32.09	33.06
2010	35.92	33.82	40.90	43.13	38.48	29.29	24.46	24.75	24.50	32.96	31.31	40.88	33.37
2011	26.71	34.32	37.71	41.27	39.95	28.93	20.34	23.40	26.38	28.22	31.85	25.89	30.41
2012	27.24	33.69	40.26	37.34	37.05	26.56	22.64	24.13	28.97	30.58	30.61	34.84	31.16
2013	32.57	33.83	34.26	38.08	34.60	24.89	22.10	20.71	25.78	26.38	29.89	30.17	29.44
2014	28.07	30.88	31.61	33.18	31.47	24.28	19.28	18.64	22.87	23.83	28.13	29.76	26.83
2015	22.55	29.94	32.93	36.68	34.90	24.50	20.75	19.13	22.90	24.50	28.67	31.77	27.44
2016	37.99	29.06	34.98	35.03	30.38	24.82	18.12	17.87	18.80	23.46	31.96	29.55	27.67
2017	29.86	36.89	35.72	35.11	30.90								
2018	28.56	31.28	35.47	38.76	33.39	27.63	20.22	20.29	22.78				
2019													
2020	34.70	32.23	36.64	32.89	34.47	25.65	22.45	21.63	25.00	26.18	27.68	28.26	28.98
2021	30.27	34.40	39.02	37.23	32.58	24.30	20.33	23.11	26.06	26.90	26.48	34.24	29.58
2022	28.56	31.91	34.67	40.66	34.16	24.26	16.37	18.40	24.25	22.53	27.88	29.05	27.73
2023	36.04	35.64						25.48	29.56	27.57	32.94	33.33	
2024	38.99	38.74	42.81	40.88	37.93	29.31	25.82	25.82	24.78	29.94	34.91	33.51	33.62

Table S8. European alpine data set monthly and annual mean ozone data. This data set includes measurements from Zugspitze, Germany (Jan. 1978 – Dec. 2023); Jungfraujoch, Switzerland (Jan 1990 – Dec. 2024) and Sonnblick, Austria (Jan 1990 – Dec. 2024).

year	Jan	Feb	Mar	Apr	May	Jun	Jul	Aug	Sep	Oct	Nov	Dec	Annual
1978	35.1	32.9	35.5	44.2	39.4	39.8	39.4	40.9	32.9	34.8	31.9	29.6	36.37
1979	27.7	32.1	38.0	43.5	46.8	47.2	44.5	38.7	39.1	32.4	28.6	28.7	37.28
1980	28.4	33.1	36.3	39.7	48.2	45.0	44.9	45.9	42.0	34.3	36.3	33.8	38.99
1981	30.3	33.2	35.5	48.1	42.9	43.4	45.8	55.6	48.5	43.1	42.8	37.8	42.25
1982	44.6	51.9	54.7	68.3	66.3	53.4	53.2	47.7	44.8	36.9	34.7	31.8	49.03
1983	34.5	34.9	44.3	45.1	50.5	56.3	57.9	59.3	47.8	42.7	40.6	37.4	45.94
1984	30.1	37.5	44.8	53.8	51.2	54.5	52.4	55.7	43.5	38.4	36.3	36.5	44.56
1985	34.2	40.5	44.7	48.9	51.6	49.2	54.7	49.9	46.5	41.0	34.6	34.2	44.17
1986	33.5	42.1	53.9	54.3	56.0	56.0	55.7	51.3	45.0	42.8	41.0	37.5	47.43
1987	38.5	38.8	46.3	58.1	59.9	51.8	57.6	48.1	44.7	40.7	39.8	41.3	47.13
1988	37.9	39.6	44.4	55.2	55.9	59.5	51.3	51.9	47.2	39.4	40.3	36.4	46.58
1989	42.0	42.0	45.9	49.7	61.0	58.7	58.3	57.4	47.5	41.0	40.9	40.4	48.73
1990	39.07	40.63	48.68	55.35	61.27	57.11	58.12	58.13	48.57	43.65	39.04	36.97	48.88
1991	40.03	41.82	45.14	52.35	52.83	50.63	55.14	54.27	47.98	43.27	40.82	40.86	47.09
1992	42.04	43.19	47.93	54.01	59.61	58.40	56.41	52.27	45.03	42.77	39.48	39.87	48.42
1993	37.65	43.78	48.75	53.74	58.11	55.89	50.93	51.56	45.64	43.48	43.01	39.84	47.70
1994	38.54	42.80	47.30	52.63	56.92	56.10	66.15	54.46	47.19	43.55	41.72	40.55	48.99
1995	40.78	46.70	47.33	52.30	58.06	56.57	61.71	58.13	47.14	47.57	42.51	41.52	50.03
1996	46.03	46.21	53.23	59.90	56.47	64.72	57.64	56.38	48.57	46.64	40.16	41.88	51.49
1997	43.66	47.19	47.46	55.83	58.96	56.86	55.10	55.18	49.89	44.88	47.53	40.11	50.22
1998	45.15	51.33	50.48	60.51	64.79	56.73	57.24	58.54	51.10	46.89	44.11	44.84	52.64
1999	45.73	47.94	53.95	62.89	59.21	61.81	59.46	54.17	52.93	47.45	43.40	43.87	52.73
2000	44.78	46.35	50.51	58.36	59.63	58.97	54.14	58.13	52.16	45.73	42.28	44.33	51.28
2001	45.72	45.51	52.23	56.98	61.04	58.91	57.42	57.11	48.05	47.23	42.50	42.82	51.29
2002	47.70	46.22	51.74	58.71	59.08	57.47	57.27	56.28	50.84	46.99	43.86	45.66	51.82
2003	44.34	49.40	55.87	60.40	59.08	62.39	62.77	66.50	56.17	48.92	43.81	43.64	54.44
2004	43.58	47.67	52.39	58.05	58.67	54.21	57.20	56.28	48.55	44.20	42.17	44.67	50.64
2005	43.58	48.09	52.69	58.39	58.58	58.53	56.94	52.32	51.14	48.49	42.23	42.76	51.15
2006	46.21	48.68	52.16	56.86	57.40	60.27	67.18	50.74	49.53	44.12	44.68	45.16	51.92
2007	42.03	47.16	52.33	61.86	57.72	58.16	54.22	55.40	47.85	47.17	42.43	44.01	50.86
2008	45.45	48.61	50.57	57.11	58.82	54.80	55.09	49.54	46.46	44.24	43.44	41.17	49.61
2009	45.63	43.12	50.43	59.91	56.00	54.96	53.33	55.23	50.68	44.00	42.88	42.38	49.88
2010	44.97	48.16	50.86	58.62	54.88	58.09	57.70	51.36	46.54	46.87	41.03	40.96	50.00
2011	45.33	49.78	55.26	58.32	58.80	52.87	55.30	52.16	49.02	46.41	47.57	41.15	51.00
2012	40.88	45.56	51.94	54.92	59.49	54.26	55.04	54.38	51.88	42.65	46.21	43.16	50.03
2013	44.68	46.53	53.79	57.91	53.10	55.96	62.08	53.98	48.66	43.96	42.72	46.31	50.81
2014	42.84	46.05	51.38	55.35	57.16	59.42	56.07	50.37	50.44	46.35	42.14	42.91	50.04
2015	43.51	47.06	51.99	55.82	55.46	57.64	61.04	59.10	50.16	45.46	43.31	47.20	51.48
2016	44.35	46.06	51.23	53.92	59.25	54.34	54.43	49.48	51.15	45.18	43.58	47.87	50.07
2017	46.66	47.46	51.51	55.02	57.58	56.66	50.61	51.28	47.74	45.98	44.16	42.96	49.80
2018	45.24	46.65	52.76	58.81	60.61	57.51	63.50	58.59	51.65	49.02	44.11	44.29	52.73
2019	43.26	48.78	51.61	57.03	55.92	59.75	57.71	52.29	46.00	43.45	43.96	45.48	50.44
2020	45.36	45.09	48.65	55.09	51.94	51.77	51.15	50.86	49.71	44.21	43.60	42.81	48.35
2021	42.90	45.00	48.51	54.50	53.91	56.69	54.29	49.78	53.58	47.76	46.22	45.19	49.86
2022	46.50	48.63	54.36	51.89	53.54	52.57	55.65	56.50	47.02	42.34	43.95	42.97	49.66
2023	44.94	48.16	50.05	52.03	54.47	62.86	53.02	49.22	50.35	45.30	43.78	45.20	49.95
2024	45.79	45.36	49.54	53.27	54.42	54.78	54.87	55.60	51.97	44.06	47.80	46.47	50.33

Table S9. European sonde data monthly and annual mean ozone data averaged over the 3 to 9 km altitude range. This data set includes measurements from Hohenpeissenberg, Germany (Jan. 1998 – Oct. 2025); Uccle, Belgium (Jan 1998 – Aug. 2025) and Payerne, Austria (Jan 1998 – June 2025).

year	Jan	Feb	Mar	Apr	May	Jun	Jul	Aug	Sep	Oct	Nov	Dec	Annual
1998	49.65	50.98	58.80	67.26	69.83	70.12	72.53	67.68	60.26	56.53	53.74	53.80	60.93
1999	51.14	58.72	59.48	67.42	64.30	69.85	73.97	63.48	60.72	52.94	53.23	50.99	60.52
2000	46.22	51.65	57.90	63.49	69.97	65.76	69.45	65.62	60.29	52.59	47.78	45.49	58.02
2001	49.65	51.84	59.79	63.17	64.80	69.96	67.83	62.69	56.73	49.21	48.20	47.11	57.58
2002	47.65	51.44	55.85	59.95	67.18	66.20	70.63	67.89	60.76	50.14	51.87	51.51	58.42
2003	54.68	54.44	57.23	64.54	69.05	68.74	72.29	70.46	61.59	56.65	47.83	49.43	60.58
2004	49.37	52.90	59.86	68.64	67.25	67.28	69.81	67.07	54.92	51.31	48.74	51.36	59.04
2005	51.36	56.55	57.97	64.50	65.03	67.60	69.71	63.81	56.91	50.34	48.83	50.55	58.60
2006	49.11	53.62	58.13	64.73	63.50	68.39	74.45	64.97	56.02	48.19	51.14	46.11	58.20
2007	46.03	50.58	61.19	65.13	64.85	72.11	67.37	67.89	63.04	53.70	54.11	52.89	59.91
2008	49.69	51.35	61.36	65.50	64.94	69.78	70.42	63.89	59.83	52.89	52.21	51.79	59.47
2009	53.16	54.66	61.61	70.32	66.41	69.64	70.56	67.65	60.86	53.76	52.67	56.18	61.46
2010	52.62	57.98	62.46	67.47	71.72	69.72	71.51	69.36	59.35	54.83	52.75	52.88	61.89
2011	53.08	55.53	59.96	63.45	65.60	73.61	71.61	64.61	57.66	52.93	48.75	47.86	59.55
2012	45.64	52.68	57.82	64.21	67.96	70.17	73.34	67.95	59.02	49.92	54.72	53.27	59.72
2013	53.17	57.14	58.65	63.95	67.19	68.12	74.99	64.64	59.11	52.41	50.43	48.56	59.86
2014	52.95	55.03	56.71	62.22	68.89	67.08	69.73	62.63	61.03	53.33	48.37	49.98	59.00
2015	49.81	53.61	55.33	62.32	68.57	67.36	70.36	68.10	58.55	53.98	52.63	49.62	59.19
2016	51.00	55.79	58.53	61.98	67.91	69.72	70.04	62.07	57.81	51.64	49.49	47.31	58.61
2017	51.49	54.20	58.28	63.67	66.30	68.08	66.13	62.23	60.24	53.28	51.07	52.30	58.94
2018	50.35	58.70	59.15	64.63	71.83	72.22	74.00	66.88	57.45	52.48	50.76	49.35	60.65
2019	53.53	50.08	58.94	65.56	66.97	70.90	66.53	60.96	56.02	50.91	53.64	50.05	58.67
2020	49.96	50.78	55.37	57.79	61.57	63.81	60.03	62.33	57.25	49.38	47.68	50.42	55.53
2021	50.90	49.77	57.09	60.17	63.57	64.89	67.01	63.04	60.10	53.12	52.00	50.71	57.70
2022	49.70	52.25	53.20	56.85	61.63	63.07	64.69	65.25	55.84	48.54	49.80	53.95	56.23
2023	52.52	49.68	57.51	62.89	66.75	75.82	69.18	66.32	58.48	52.97	55.11	50.01	59.77
2024	51.09	49.73	55.97	64.09	66.75	70.10	74.10	68.88	65.21	53.69	54.03	52.44	60.51
2025	52.31	52.99	58.19	63.11	64.40	67.09	65.59	64.29	52.45	52.92			